ACSNANO

www.acsnano.org

ARTICLE

Room-Temperature Gate Voltage Modulation of Plasmonic Nanolasers

Zhen-Ting Huang, Ting-Wei Chien, Chang-Wei Cheng, Cheng-Ching Li, Kuo-Ping Chen, Shangjr Gwo, and Tien-Chang Lu*

Cite This: *ACS Nano* 2023, 17, 6488−6496

Read Online

ACCESS | Metrics & More | Article Recommendations | Supporting Information

ABSTRACT: **Stable electrical modulation of plasmonic nanolasers is achieved on a hybrid graphene−insulator−metal (GIM) platform at room temperature. To support surface plasmon polariton (SPP) resonance, a zinc oxide (ZnO) nanowire is placed on the GIM platform to create a plasmonic cavity with a compact mode volume of $2.6 \times 10^{-2}\ \lambda^3$, and the graphene layer is used as a transparent electrode for electrical modulation. When a gate voltage is applied, the surface electron density of Al varied, which results in the shifting of its plasma frequency and thus affects its SPP dispersion. In particular, this variation strongly changes the internal loss of the SPP mode; thus, the lasing thresholds of the ZnO nanowire plasmonic nanolasers on the GIM platform can be modulated by the gate voltage. This study demonstrates the gate voltage modulation of ZnO nanowire plasmonic nanolasers on a GIM platform at room temperature. These nanolasers can exhibit ultrahigh modulation speed on the order of terahertz. Accordingly, plasmonic nanolasers with gate voltage modulation have high potential for plasmonic circuit applications with high operation speed and versatility.**

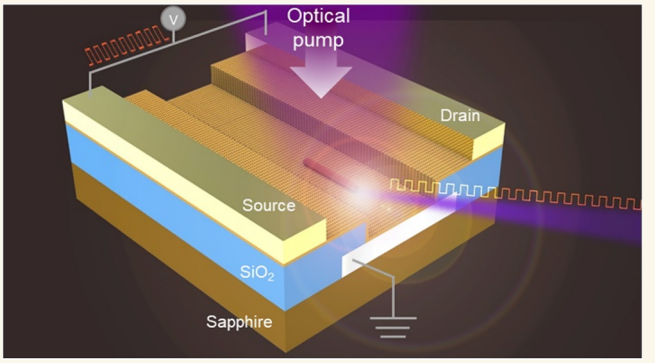

KEYWORDS: *graphene, nanolaser, electrical gating, high-speed modulation, surface plasmon polariton*

INTRODUCTION

The demand for nanoscale optoelectronics has increased dramatically in recent years. Suitable nanoscale optical devices are required for achieving improved functionality and reduced power consumption in several cutting-edge applications such as photonic integrated circuits (PICs) and quantum communications.[1−4] However, the optical diffraction limit restricts the development of nanoscale optical devices. A promising method for breaking the optical diffraction limit is the use of surface plasmons (SPs).[5−7] SPs are localized electromagnetic fields induced by the collective oscillation of surface electrons, and they are formed at the interface between a dielectric and a metal.[5−7] When SPs couple with incident photons, quasiparticles called surface plasmon polaritons (SPPs) are formed on the metal surface.[6] These quasiparticles can be confined with an ultrasmall mode volume and thus high potential for use in nanoscale optical devices. SPPs have been applied in many devices, including plasmonic photodetectors,[8,9] surface plasmon resonance sensors,[10,11] nanoscale optical tweezers,[12,13] and nanolasers.[14−16] For plasmonic nanolasers, SPPs provide an ultracompact laser cavity, and their small mode volume and high group index lead to a strong Purcell effect.[17−19] A strong Purcell effect can enhance light−matter interactions, engender a laser cavity with a low lasing threshold, and afford a high operation speed.[17] With these powerful capabilities, some groups have even proposed the plasmonic laser that can be electrically driven at room temperature.[20] Furthermore, strong light−matter interactions cause a plasmonic nanolaser to be sensitive to variations in the characteristics of the laser cavity, which implies that the lasing signal can be modulated by tuning the cavity geometry or material. The modulation of plasmonic nanolasers has been realized through many approaches, such as hot-electron transfer,[21] spectral engineering of gain materials,[22] and Lorentzian reciprocity disruption.[23] Therefore, plasmonic nanolasers have potential for improving the performance of conventional PICs and architecting on-chip plasmonic circuits,

Received: November 23, 2022
Accepted: March 27, 2023
Published: March 29, 2023

https://doi.org/10.1021/acsnano.2c11716
ACS Nano 2023, 17, 6488−6496

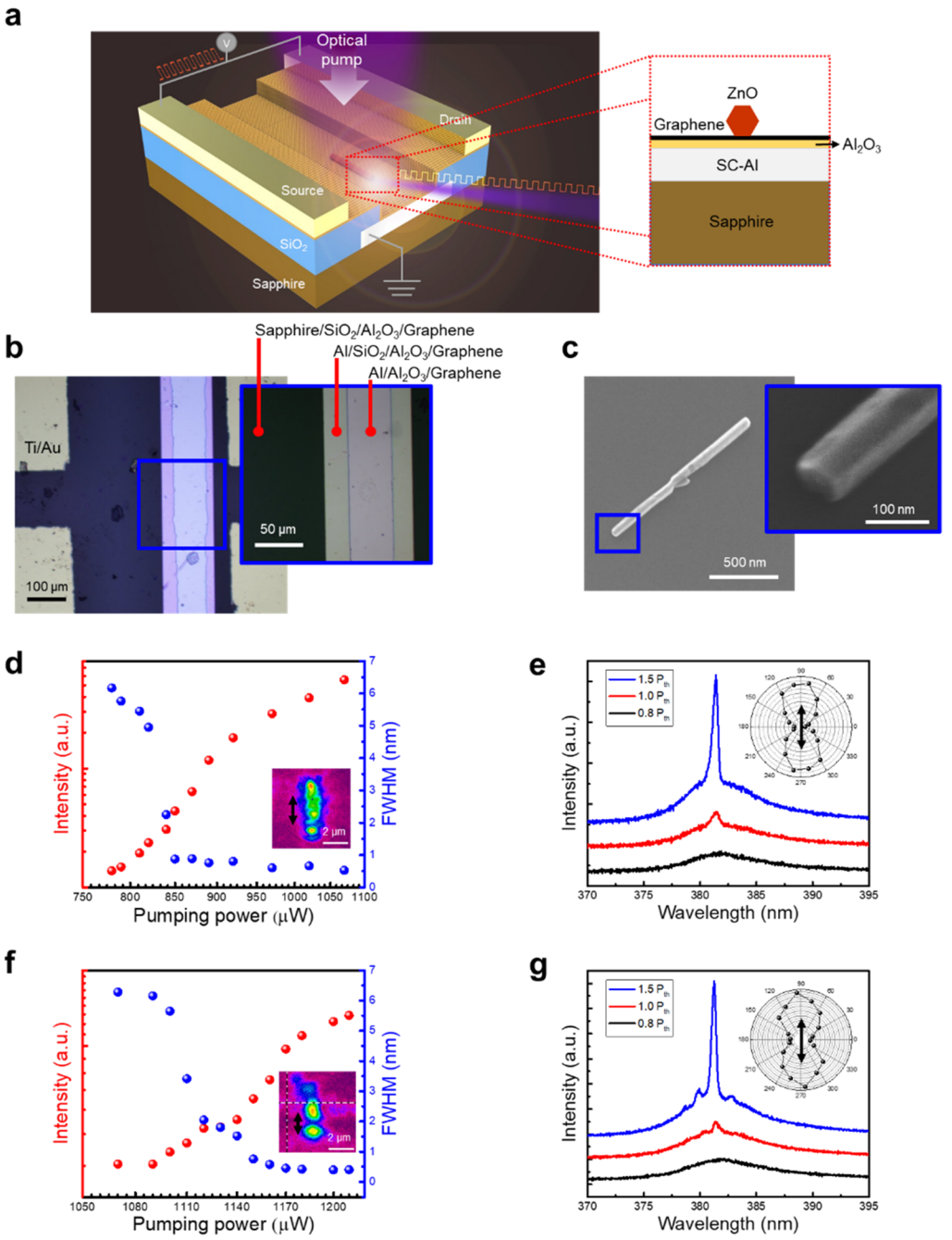

Figure 1. Schematics and lasing characteristics of the ZnO nanowire plasmonic nanolasers on a GIM platform. (a) Schematics of the gate modulation of the nanolaser (the inset shows the cross section of the laser). The voltage drop is applied between the source/drain connected to the graphene layer and the gate electrodes. (b) Optical microscopy image of the GIM structure. (c) Scanning electron microscopy image of the ZnO nanowire. (d) L−L curves and (e) power-dependent PL spectra of a ZnO nanowire plasmonic nanolaser with a 7 nm thick Al_2O_3 layer. (f) L−L curves and (g) power-dependent PL spectra of a ZnO nanowire plasmonic nanolaser with a 15 nm thick Al_2O_3 layer. The insets of (d) and (f) depict the corresponding near-field images, and the insets of (e) and (g) depict the corresponding far-field polarization. The black arrows in the insets indicate the orientation of the ZnO nanowire.

which are crucial for the development of nanoscale optical devices.

In order to construct an actively modulated plasmonic nanolaser, single-layer graphene (SLG) can be a perfect component that has suitable interactions with SPPs owing to its one-atom thickness. Because of the massless Dirac fermions produced in graphene through Dirac cone dispersion at K valleys, graphene has ultrahigh electron mobility and can be used as a transparent electrode to support electrical injection.[24−26] Graphene also has high mechanical strength and thermal conductivity,[27−29] which allow it to be used in many manufacturing processes and room-temperature operations. Moreover, graphene is a promising candidate for realizing SPP modulation. Kim et al. demonstrated the electrically controlled plasmon resonance of gold nanorods in a hybrid graphene−nanorod structure.[30] They achieved SPP modulation through top electrolyte gating. When a gate voltage was applied, the Fermi level of graphene shifted, thus switching

https://doi.org/10.1021/acsnano.2c11716
ACS Nano 2023, 17, 6488−6496

on or off its interband transition. According to the Kubo formula, variations in the interband transition strongly affect the dielectric functions of graphene and thus affect the resonant frequency and quality factor of gold plasmons in the hybrid graphene−nanorod structure. A similar electrical modulation has been demonstrated in a photonic crystal defect laser and band-edge laser.[31,32] However, in the visible or ultraviolet (UV) region, the Kubo formula becomes invalid because a strong excitonic effect occurs near the saddle-point singularity at the M point, and the gate-induced Fermi-level shift of graphene does not cause a large variation in the dielectric function. Accordingly, our previous study proposed a hybrid graphene−insulator−metal (GIM) platform for realizing SPP modulation at 373 nm.[33] The combination of graphene with a metal prompted graphene to exhibit p- or n-type doping because of the difference in work function between graphene and the metal. The difference in work function influenced the surface carrier density of the metal and shifted its plasma frequency; thus, the internal loss of the SPP mode changed. The aforementioned study indicated that the lasing threshold of a zinc oxide (ZnO) nanowire plasmonic nanolaser could be reduced by 50% when SLG was combined with an Al template and separated by a 7 nm thick Al_2O_3 layer. In another study, we used the GIM platform to realize the current modulation of a ZnO nanowire plasmonic nanolaser at 77 K by inducing a Doppler shift and breaking the Lorentzian reciprocity.[23] Moreover, we have realized room-temperature current modulation in 2021.[34] Although the electrical modulation of plasmonic nanolasers has been achieved at room temperature, severe current-induced thermal accumulation occurs during this modulation, and the nanowire must be carefully aligned with the current direction, which can affect the modulation performance and increase the fabrication complexity.

The present study demonstrated the active modulation of ZnO nanowire plasmonic nanolasers on a GIM platform by applying a gate voltage. Achieving modulation through electrical gating entails generating an electric field in the gate oxide and then inducing charge concentration in graphene and the metal. Therefore, when a gate voltage is applied, the carrier density of graphene changes, which leads to a shift in its Fermi level. Subsequently, graphene would exhibit p- or n-type doping depending on whether the shifted Fermi level crosses the Dirac point. The Fermi level of graphene on the GIM platform deviates from the Dirac point even in the absence of a gate voltage because of the difference in the work functions of graphene and the metal.[33] The variation in the carrier density of graphene can be examined through Raman scattering analysis.[35] The positions of the G and 2D peaks in the Raman spectra of graphene are sensitive to changes in the charge concentration. The shifts of these two peaks can determine the doping or charge concentration characteristic of graphene. Therefore, in the present study, Raman scattering analysis was performed to determine the gate-induced doping dependence of graphene on the GIM platform. This information can be used to determine the variation in the surface carrier density of the metal, which is correlated with the Fermi-level shift of graphene. Furthermore, gate-voltage-induced variations in the surface carrier density of the metal could cause a shift in the plasma frequency of the metal and significantly affect the internal loss of the SPP mode. With this feature, the gate modulation of a ZnO nanowire plasmonic nanolaser can be achieved. The application of a gate voltage can considerably reduce the thermal accumulation observed in current modulation[23] and thus improve the modulation performance and enable stable room-temperature operation. Gate voltage application is a promising method for the integration of a light source and an optical modulator, which can facilitate the development of plasmonic circuits and increase the degrees of freedom in optical system design.

RESULTS AND DISCUSSION

Figure 1a illustrates a schematic of the gate-modulated ZnO nanowire plasmonic nanolaser on the GIM platform. To construct the back-gate configuration shown in Figure 1a, a single-crystalline Al film was grown using molecular-beam epitaxy and then etched through deep UV lithography and a wet-etching process to form an Al strip on a sapphire substrate. The flatness of the prepared Al film prevented surface scattering in the SPP mode.[36] An atomic force microscopy (AFM) image of the Al strip on the sapphire substrate is depicted in Figure s1c in the Supporting Information, and the root-mean-square (RMS) roughness of the Al strip was measured to be 0.754 nm. Plasma-enhanced chemical vapor deposition was conducted to grow a 300 nm thick SiO_2 layer on both sides of the Al strip to support the deposition of electrodes. To ensure the insulation of the gate oxide, atomic layer deposition was performed to grow an Al_2O_3 layer, and SLG was then transferred to construct the GIM platform. An AFM image of the configuration obtained after the transfer of graphene is illustrated in Figure s1d, and the RMS roughness of this configuration was 1.16 nm. Finally, a ZnO nanowire was placed on the GIM platform to form a plasmonic cavity, and electrodes were deposited on the source, drain, and gate of the platform for electrical modulation control. The right inset of Figure 1a depicts the cross section of the ZnO nanowire plasmonic nanolaser. When a gate voltage was applied, the charge concentrations in graphene and Al varied with the thickness of the Al_2O_3 layer, which determined the capacitance of the GIM structure. Accordingly, to explore the electrical gating effect, two samples with different Al_2O_3 layer thicknesses (i.e., 7 and 15 nm) were prepared. The electrical properties of these samples for different electrode lengths are shown in Figure s1b. Figure 1b illustrates the optical microscopy image of the GIM platform; in this figure, the left and right electrodes are the source and drain, respectively, and the distance between these electrodes was 45 μm. A scanning electron microscopy image of the prepared ZnO nanowire is displayed in Figure 1c. The side length and wire length were approximately 45 nm and 1.5 μm, respectively. Moreover, a 355 nm pulse laser with a repetition rate of 1 kHz and a pulse duration of 0.5 ns was used to pump the ZnO nanowire plasmonic nanolasers at room temperature. The corresponding light-in versus light-out (L−L) curves and power-dependent photoluminescence (PL) spectra obtained in the absence of a gate voltage are illustrated in Figure 1d−g. Measurement results obtained using the 7 nm thick Al_2O_3 layer are presented in Figure 1d,e, and those obtained using the 15 nm thick Al_2O_3 layer are presented in Figure 1f,g. According to the L−L curves, the lasing threshold of the ZnO nanowire plasmonic nanolaser with the 7 nm thick Al_2O_3 layer was lower than that of the ZnO nanowire plasmonic nanolaser with the 15 nm thick Al_2O_3 layer. This result was observed because the nanolaser with the 7 nm thick Al_2O_3 layer had a stronger plasmon-enhanced Purcell effect than did the nanolaser with the 15 nm thick Al_2O_3 layer,[16] and the lasing line width was

https://doi.org/10.1021/acsnano.2c11716
ACS Nano 2023, 17, 6488−6496

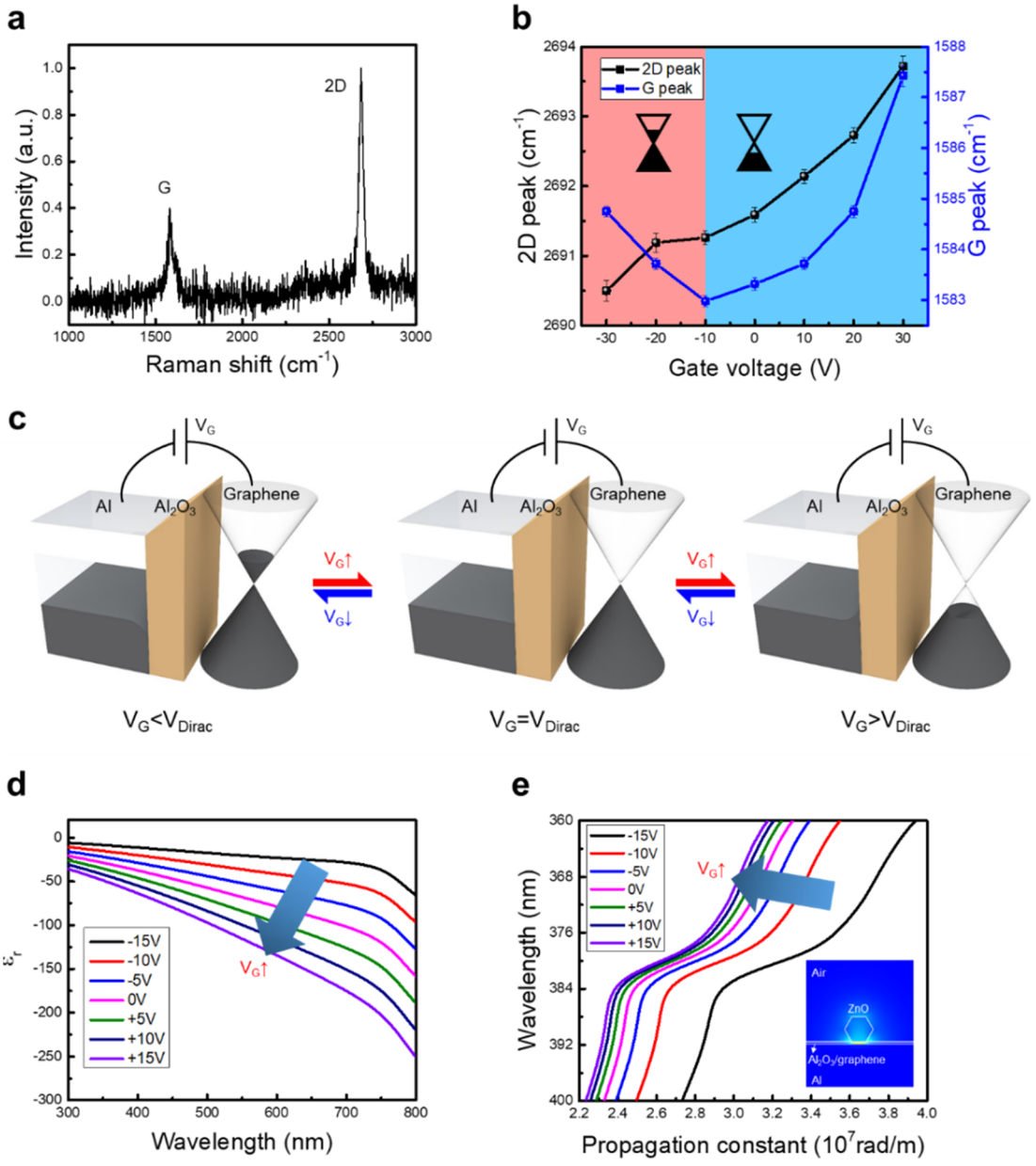

Figure 2. Variations in the Raman scattering of graphene and the SPP characteristics with the gate voltage (V_G). (a) Raman spectrum of graphene in the absence of a gate voltage. (b) Shifts in the G and 2D peaks of graphene with V_G, where the red and blue regions represent the n- and p-type doping of graphene, respectively. (c) Variations in the charge concentration in graphene and the metal with V_G, where V_{Dirac} is the voltage corresponding to the Dirac point. (d) Real part of the permittivity spectra of Al covered with a 7 nm thick Al_2O_3 layer and graphene under different V_G. (e) Dispersion curves for the SPP mode under different V_G. The inset of (e) illustrates the electric field distribution of the SPP mode when a gate voltage was not applied.

approximately 0.5 nm for both lasers. As indicated in the insets in the power-dependent PL spectra, the far-field polarization of these lasers was parallel to the orientations of their ZnO nanowires, which corresponds to the transverse magnetic polarization and meets the characteristic of the fundamental SPP mode.[16]

Before examining the gate modulation of the ZnO nanowire plasmonic nanolasers, this study investigated the Fermi-level shift of graphene by measuring its Raman scattering. Figure 2a displays the Raman spectrum of the SLG on the GIM platform. This spectrum contained two notable peaks. The peak located at the lower Raman shift was ascribed to the G peak, and the other peak was ascribed to the 2D peak. Moreover, the aforementioned spectrum did not contain a D peak, indicating that the prepared graphene had perfect zigzag edges, which suggested that the graphene had high quality and was nearly free of defects.[37,38] When a gate voltage was applied to the GIM platform, the G and 2D peaks began to shift, as illustrated in Figure 2b. Notably, when the gate voltage increased from negative to positive gate bias, the 2D peak always exhibited a blue shift; however, the G peak initially exhibited a red shift and then exhibited a blue shift at gate voltages higher than −10 V. This difference originated from the change in the charge concentration in graphene. The blue shift of the 2D peak was engendered by the decrease in the electron concentration and the increase in the hole concentration, and the shift of the G peak was engendered by the deviation of the Fermi level from the Dirac point.[35] Therefore, the blue shift of the 2D peak

https://doi.org/10.1021/acsnano.2c11716
ACS Nano 2023, 17, 6488−6496

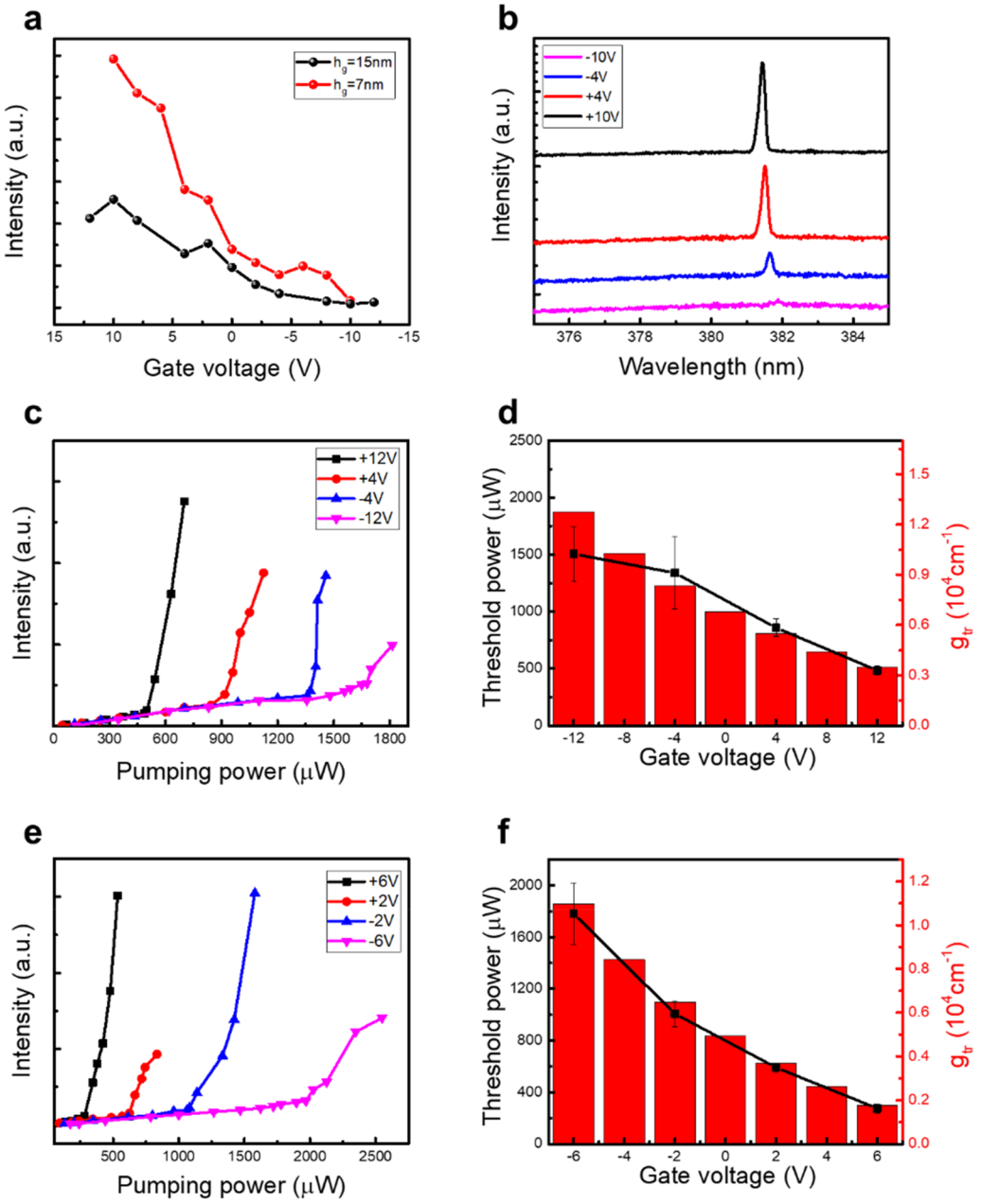

Figure 3. Gate voltage modulation of nanolasers on a GIM platform. (a) Lasing peak intensities of nanolasers with 7 nm thick layer and 15 nm thick Al_2O_3 layers as a function of V_G. The pumping power was fixed right above the threshold when the gate voltage is 10 V. (b) Gate-voltage-dependent PL spectra of the nanolaser with the 7 nm thick Al_2O_3 layer at a pumping power right above the threshold when the gate voltage is 10 V. (c) L−L curves and (d) corresponding threshold power of the nanolaser with the 15 nm thick Al_2O_3 layer under different V_G. (e) L−L curves and (f) corresponding threshold power of the nanolaser with the 7 nm thick Al_2O_3 layer under different V_G. The black dots in (d) and (f) indicate the measured threshold power under different V_G. The red bars in (d) and (f) indicate the simulated transparency threshold gain (g_{tr}) of the SPP mode.

when the gate voltage was increased from −30 to 30 V implied that the p-type doping of graphene increased with the gate voltage. Moreover, the lowest Raman shift of the G peak indicated that the Fermi level of graphene was located at the Dirac point, and the shift of the G peak changed with the gate voltage because the Fermi level crossed the Dirac point. Figure 2c displays the variations in the charge concentrations in graphene and the metal with the gate voltage. In this figure, V_{Dirac} is the gate voltage (V_G) corresponding to the Dirac point. When V_G was gradually increased to V_{Dirac}, as indicated in the red region in Figure 2b, the electron concentration decreased, which resulted in the Fermi level of graphene approximating the Dirac point. Therefore, a blue shift occurred in the 2D peak but a red shift occurred in the G peak. In the aforementioned region, graphene still exhibited n-type doping, which weakened as V_G increased. Based on the capacitor discharge effect, the gate-induced n-type doping of graphene led to a reduction in the surface electron density of Al, which caused the plasma frequency of Al to be lower than that at thermal equilibrium. When V_G reached V_{Dirac}, the Fermi level of graphene was located at the Dirac point; thus, the G peak exhibited the lowest Raman shift. Graphene also exhibited

https://doi.org/10.1021/acsnano.2c11716
ACS Nano 2023, 17, 6488−6496

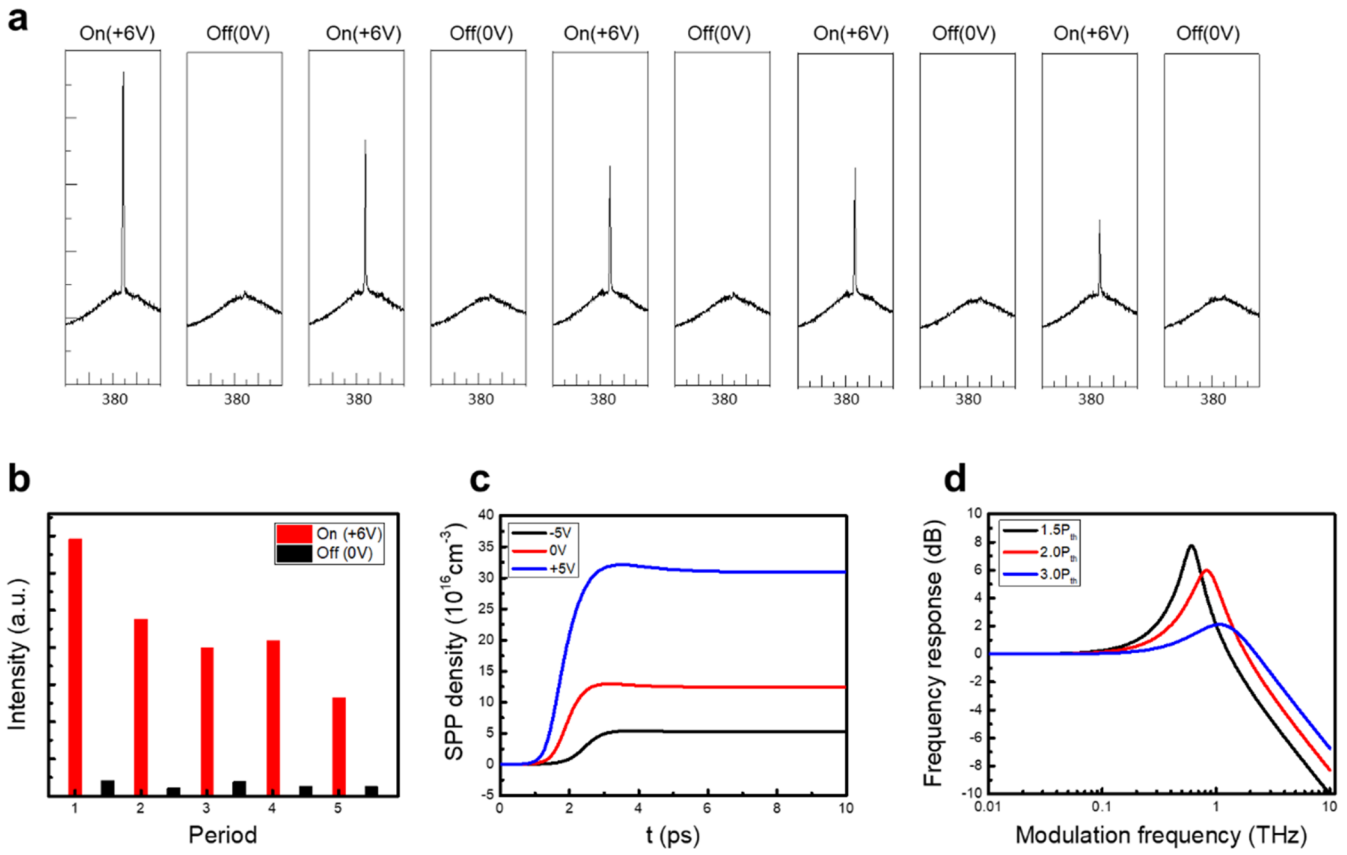

Figure 4. Repeatability measurements and dynamics of a ZnO nanowire plasmonic nanolaser with a 7 nm thick Al_2O_3 layer. (a) Spectra and (b) corresponding peak intensities obtained in the repeatability test over five periods, where V_G was 6 and 0 V in the on-state and off-state, respectively, and the switching period was 1 s. (c) Turn-on behavior of the nanolaser under different V_G; time t = 0 represents the time when the operation of the pumping laser was started. (d) Small-signal frequency response of the nanolaser under different pumping power densities.

charge neutrality; thus, no changes occurred in the surface electron density or plasma frequency of Al. At gate voltages higher than V_{Dirac}, as indicated in the blue region in Figure 2b, an increase in the hole concentration resulted in the blue shifts of the 2D and G peaks because the Fermi level gradually moved away from the Dirac point. Consequently, graphene exhibited p-type doping, and electrons accumulated on the Al surface because of the gate-induced electric field in the gate oxide, which increased the surface electron density and changed the plasma frequency. Notably, without V_G, graphene still exhibited p-type doping (Figure 2b) because of the work function difference between graphene and Al. This result is in agreement with the finding of a previous study.[33]

To examine the effect of the gate voltage on the SPP mode, the gate-induced variation in the electron density of graphene was determined using the following equation:[35,39]

$$\Delta n = C_{ox}(V_{Dirac} - V_G)/e \quad (1)$$

where n is the surface electron density, and C_0 is the capacitance of the gate oxide, which can be calculated by the ratio of the permittivity and thickness of the gate oxide. V_{Dirac} (−10 V in Figure 2b) can be determined by measuring the Raman scattering of graphene. Based on the electrical gating effect, the change in the surface electron density of Al can be estimated using $-\Delta n$. Moreover, in the absence of a gate voltage, the p-type doping of graphene on the GIM platform increased the surface electron density of Al by 1.7 times.[33] Accordingly, the gate-induced variation in the plasma frequency can be derived using the Drude−Lorentz model, and a fine-element method can be used to estimate the shift in the SPP dispersion. Figure 2d illustrates the real part of the permittivity spectrum of Al under increasing V_G. When V_G was increased from −15 to 15 V, the real part of the permittivity of Al decreased, which resulted from the plasma frequency of Al changing by approximately 0.806−1.658 times its initial value. By substituting the gate-controlled permittivity of Al into the simulation model, the gate modulated characteristics of the SPP mode can be calculated. Figure 2e presents the SPP dispersion of the ZnO nanowire plasmonic nanolasers under increasing V_G, and the inset shows the electric field distribution of the SPP mode, whose electric field is primarily localized in the gate oxide. Note that a Lorentzian gain was considered in the dielectric function of the ZnO nanowire, and the mode volume of the nanolaser with the 7 nm thick Al_2O_3 layer was estimated to be only $2.6 \times 10^{-2}\ \lambda^3$. As V_G increased, the plasma frequency of Al increased and caused the resonant frequency of the SPP mode to move away from the PL range of the ZnO nanowire, which weakened the SPP resonance and led to a considerable reduction in the SPP momentum. The localization of the SPP mode also decreased as V_G increased, indicating that the electric field gradually shifted away from the metal surface; thus, the internal loss decreased. These results indicate that the threshold gain of the ZnO nanowire plasmonic nanolasers was modulated by the gate voltage, and the higher the applied gate voltage was, the lower the lasing threshold became.

https://doi.org/10.1021/acsnano.2c11716
ACS Nano 2023, 17, 6488−6496

Figure 3a displays the gate-modulated peak intensity of the ZnO nanowire plasmonic nanolasers with the 7 nm thick Al_2O_3 layer and 15 nm thick Al_2O_3 layer on the GIM platform. The pumping power was fixed at right above the threshold when the gate voltage is 10 V. When a gate voltage was applied, the peak intensities of both nanolasers were clearly attenuated; the intensity variation was higher for the laser with the 7 nm thick Al_2O_3 layer than for that with the 15 nm thick Al_2O_3 layer. This difference originated from the capacitances of the aforementioned lasers. Based on eq 1, the laser with the thinner gate oxide had a larger capacitance, which led to a more significant change in the surface electron density. Figure 3b illustrates gate-voltage-dependent PL spectra of the nanolaser with the 7 nm thick Al_2O_3 layer at a fixed pumping power right above the threshold when the gate voltage is 10 V. A notable peak was observed in the spectra at 10 V, and the PL intensity gradually decreased with V_G. To quantify this gate-induced PL attenuation, L−L curves were measured for different V_G, and the threshold power was extracted. For the nanolaser with the 7 nm thick Al_2O_3 layer, even a small gate voltage induced a large variation in the threshold power, as shown in Figure 3e,f. The threshold power of this laser increased from 275 to 1780 μW (nearly a 6.5-fold increase) as V_G decreased from 6 to −6 V. This increase in the threshold power indicates that the aforementioned laser has excellent modulation performance and is suitable for practical application. By contrast, the threshold power of the nanolaser with the 15 nm thick Al_2O_3 layer increased by only approximately 3.1-fold as V_G decreased from 12 to −12 V. To compare the gate-modulated threshold power of the two nanolasers, the transparency threshold gain (g_{tr}) was calculated by dividing the internal loss by the waveguide confinement factor (red bars in Figure 3d,f). In the plasmonic cavities of these nanolasers, the modal loss was dominated by the internal loss because the cavity was sufficiently long for neglecting the mirror loss. In our calculation, the g_{tr} of the nanolaser with a 15 nm thick Al_2O_3 layer increases around 3.6-fold from +12 V to −12 V, and that with a 7 nm thick Al_2O_3 layer increases around 6.3-fold from +6 V to −6 V. These results exhibited good fits with the measurement results, becoming pivotal evidence for proving the modulation mechanism. These results suggest that the gate modulation of the ZnO nanowire plasmonic nanolasers was realized on the GIM platform. The excellent modulation performance of these lasers indicates the robustness of the modulation mechanism and the potential for integrating these lasers with optical modulators.

To test the reliability of the gate modulation, repeatability measurements were performed using the ZnO nanowire plasmonic nanolaser with the 7 nm thick Al_2O_3 layer on the GIM platform. Figure 4a presents the PL spectra modulated by switching V_G between 6 and 0 V. At 6 V, a lasing peak was noted in the PL spectrum when the pumping power was set to 1.5 times the threshold power when the gate voltage is 6 V. As soon as V_G was turned off, the lasing peak disappeared. Subsequently, continue to turn on V_G at +6 V, and the lasing peak recovered. The variations in the peak intensity of this laser after testing for five periods are illustrated in Figure 4b, where each period contained an on-state and off-state, and the switching period was 1 s. Notably, the lasing peak was always recovered in each on-state and nearly disappeared in the off-state. In the on-state, a positive gate bias caused surface electrons to accumulate at the metal surface, which increased the plasma frequency of the metal and decreased the internal loss of the SPP mode. Consequently, at a fixed pumping power, the lasing signal could be dynamically modulated by switching on and switching off V_G. Results similar to the aforementioned ones were obtained for the nanolaser with the 15 nm thick Al_2O_3 layer (Figure s3). However, after a few periods, a decay in the peak intensity still occurred because of the thermal accumulation that was possibly caused by the leakage current. This phenomenon is not evident in Figure s3 because of the relatively strong insulating capability of the 15 nm thick Al_2O_3 layer.

The turn-on behavior and small-signal frequency resonance of the nanolasers on the GIM platform were calculated using the following rate equations:[40]

$$\frac{dn_A}{dt} = \eta P - \frac{n_A}{\tau_{AB}} \tag{2}$$

$$\frac{dn_B}{dt} = \frac{n_A}{\tau_{AB}} - An_B - Fv_g\frac{a(n_B - n_{tr})}{1 + \varepsilon s}s \tag{3}$$

$$\frac{ds}{dt} = \Gamma\beta An_B + \Gamma Fv_g\frac{a(n_B - n_{tr})}{1 + \varepsilon s}s - \gamma s \tag{4}$$

where n_A, n_B, n_{tr}, and s are the reservoir exciton density, ground-state exciton density, transparency carrier density, and SPP density, respectively. P denotes the pumping power density; η denotes the injection efficiency; τ_{AB} denotes the lifetime of exciton transition from the exciton reservoir to the exciton ground state; and Γ, β, F, and v_g denote the waveguide confinement factor, spontaneous emission coupling factor, Purcell factor, and group velocity of the SPP mode, respectively. Moreover, γ represents the loss rate of the SPP mode; a represents the differential gain of the ZnO nanowire; ε represents the gain saturation coefficient, which indicates that the optical gain is saturated in the linear region when the exciton density increases; and A represents the spontaneous emission rate, which can be estimated from F/τ_r, where τ_r is the spontaneous emission lifetime of the ground state exciton. Solving the simultaneous differential equations presented in eqs 2−4 yielded the turn-on behavior of the nanolasers. The detailed parameters of these nanolasers are presented in Table s1. When a gate voltage is applied, the modulated internal loss of the SPP mode engendered a change in its loss rate, affecting the turn-on dynamics of the laser cavity. Figure 4c illustrates the turn-on behavior of the nanolaser with the 7 nm thick Al_2O_3 layer under different V_G. The time t = 0 represents the time when the pumping laser begins functioning. A lower V_G resulted in a slower increase in the SPP density because of the higher threshold that must be reached by the exciton density. Nevertheless, the turn-on delay and rise time of the aforementioned nanolaser were within 2 and 1 ps, respectively. Such a short turn-on delay was caused by the compact cavity of the plasmonic nanolaser. The modulation frequency of the laser could be also estimated using eqs 2−4. Figure 4d displays the small-signal frequency responses induced by gate modulation at different pumping power densities when the aforementioned laser was modulated by a small sinusoidal gate voltage. When the pumping power density was increased to 3 times the threshold power density, the modulation frequency for the largest frequency response was of the order of a few terahertz, signifying that the nanolaser with the 7 nm thick Al_2O_3 layer had a high modulation speed. This fast modulation capability was ascribed to the strong Purcell effect for this laser

https://doi.org/10.1021/acsnano.2c11716
ACS Nano 2023, 17, 6488−6496

and the extremely short photon lifetimes in its plasmonic cavities, causing the SPP mode to be sensitive to variations from the electrical modulation. Because of its excellent characteristics, the ZnO nanowire plasmonic nanolaser with the 7 nm thick Al_2O_3 layer was determined to be suitable for developing on-chip plasmonic circuits and realizing high-speed data processing.

CONCLUSION

This study achieved the dynamic modulation of ZnO nanowire plasmonic nanolasers on a GIM platform at room temperature. When a gate voltage was applied to the GIM structure, the charge concentrations in graphene and Al depended on the gate bias, which influenced the intrinsic optical properties of Al and oscillations of the SPP mode. By examining the G and 2D peaks of graphene in the Raman spectrum, the doping type of graphene can be determined, and then the change of surface electrons in Al can be also realized. The varied surface electron density of Al led to a shift in its plasma frequency and thus affected the SPP dispersion and internal loss. Consequently, the lasing thresholds of the nanolasers were modulated by applying a gate voltage. As the applied gate voltage decreased from 6 to −6 V, the threshold power of the ZnO nanowire plasmonic nanolaser with a 7 nm thick Al_2O_3 layer increased by 6.5-fold, demonstrating excellent modulation performance. Moreover, after repeatability measurements, this nanolaser exhibited robustness for gate modulation, which enabled it to realize stable room-temperature operation. Calculations of the turn-on dynamics and small-signal frequency responses of the aforementioned nanolaser indicated that its modulation speed was of the order of a few terahertz. Because of its high-speed modulation capability, the nanolaser with the 7 nm thick Al_2O_3 layer has high potential for use in on-chip plasmonic circuits and improving its operating speed.

EXPERIMENTAL SECTION

Optical Measurement Setup. The constructed nanolasers were pumped using a 355 nm NdYVO4 pulse laser with a repetition rate of 1 kHz and a pulse duration of 0.5 ns at room temperature. A 100× infinity-corrected objective lens was also used with a working distance and numerical aperture of 11 mm and 0.55, respectively. The diameter of the pumping spot was approximately 1 μm. The gate voltage was provided by a power supply (Keithley 238). The Raman scattering was measured using the NT-MDT NTEGRA spectra system that performs confocal Raman imaging. In confocal Raman spectroscopy, the sample was pumped using a 532 nm continuous-wave laser, and a 100× objective lens with a numerical aperture of 0.7 was used to collect the scattered light. The detection was performed using a thermoelectrically cooled charge-coupled device that was attached to a 520 mm long spectrometer.

Simulations of Laser Characteristics. Different aspects, including dispersion curves, internal losses, and electric field distributions, were simulated using the finite element software COMSOL Multiphysics. In the simulation model, the side length of the ZnO nanowire was 45 nm, and the thickness of the Al_2O_3 layer was 15 and 7 nm (corresponding to the results in Figure 3d and Figure 3f, respectively).

ASSOCIATED CONTENT

Supporting Information

The Supporting Information is available free of charge at https://pubs.acs.org/doi/10.1021/acsnano.2c11716.

Images of our devices on the PCB, electrical properties of the graphene, surface morphology, temperature-dependent lasing spectra of the ZnO nanowire on the GIM platform, repeatability measurement of the ZnO nanowire plasmonic nanolaser with a thicker gate oxide, mode profile of the ZnO nanowire plasmonic nanolaser, intrinsic properties of the ZnO nanowire, optical characteristics of the ZnO nanowire lying on the sapphire substrate, energy confinement factor of each material in the ZnO nanowire plasmonic nanolaser, gate modulation of the ZnO wire laser on a thickened GIM structure, Q factor of the ZnO nanowire plasmonic nanolaser, and a table indicating the parameters we applied in the rate equations (PDF)

AUTHOR INFORMATION

Corresponding Author

Tien-Chang Lu − *Department of Photonics, College of Electrical and Computer Engineering, National Yang Ming Chiao Tung University, Hsinchu 30010, Taiwan;* orcid.org/0000-0003-4192-9919; Email: timtclu@nycu.edu.tw

Authors

Zhen-Ting Huang − *Department of Photonics, College of Electrical and Computer Engineering, National Yang Ming Chiao Tung University, Hsinchu 30010, Taiwan;* orcid.org/0000-0002-2912-1469

Ting-Wei Chien − *Department of Photonics, College of Electrical and Computer Engineering, National Yang Ming Chiao Tung University, Hsinchu 30010, Taiwan*

Chang-Wei Cheng − *Department of Physics, National Tsing Hua University, Hsinchu 30013, Taiwan;* orcid.org/0000-0001-8937-5084

Cheng-Ching Li − *Department of Photonics, College of Electrical and Computer Engineering, National Yang Ming Chiao Tung University, Hsinchu 30010, Taiwan*

Kuo-Ping Chen − *Institute of Photonics Technologies, National Tsing Hua University, Hsinchu 30013, Taiwan*

Shangjr Gwo − *Department of Physics, National Tsing Hua University, Hsinchu 30013, Taiwan;* orcid.org/0000-0002-3013-0477

Complete contact information is available at: https://pubs.acs.org/10.1021/acsnano.2c11716

Notes

The authors declare no competing financial interest.

ACKNOWLEDGMENTS

The authors thank Prof. Tzy-Rong Lin from National Taiwan Ocean University and Prof. Chan-Shan Yang from National Taiwan Normal University for their contributions to fruitful discussions. This work was financially supported by Taiwan's National Science and Technology Council under Contracts MOST 110-2221-E-A49-058 -MY3 and MOST 110-2622-8-A49-008-SB.

REFERENCES

(1) Cozzolino, D.; Da Lio, B.; Bacco, D.; Oxenløwe, L. K. High-Dimensional Quantum Communication: Benefits, Progress, and Future Challenges. *Adv. Quantum Technol.* **2019**, *2*, 1900038.

(2) Gisin, N.; Thew, R. Quantum communication. *Nat. Photonics* **2007**, *1*, 165−171.

(3) Nagarajan, R.; Joyner, C. H.; Schneider, R. P.; Bostak, J. S.; Butrie, T.; Dentai, A. G.; Dominic, V. G.; Evans, P. W.; Kato, M.;

Kauffman, M.; Lambert, D. J. H.; Mathis, S. K.; Mathur, A.; Miles, R. H.; Mitchell, M. L.; Missey, M. J.; Murthy, S.; Nilsson, A. C.; Peters, F. H.; Pennypacker, S. C.; Pleumeekers, J. L.; Salvatore, R. A.; Schlenker, R. K.; Taylor, R. B.; Tsai, H.-S.; Van Leeuwen, M. F.; Webjorn, J.; Ziari, M.; Perkins, D.; Singh, J.; Grubb, S. G.; Reffle, M. S.; Mehuys, D. G.; Kish, F. A.; Welch, D. F. Large-scale photonic integrated circuits. *IEEE J. Sel. Top. Quantum Electron.* **2005**, *11*, 50−65.

(4) Davis, T. J.; Gómez, D. E.; Roberts, A. Plasmonic circuits for manipulating optical information. *Nanophotonics* **2016**, *6*, 543−559.

(5) Barnes, W. L.; Dereux, A.; Ebbesen, T. W. Surface plasmon subwavelength optics. *Nature* **2003**, *424*, 824−830.

(6) Zayats, A. V.; Smolyaninov, I. I.; Maradudin, A. A. Nano-optics of surface plasmon polaritons. *Phys. Rep.* **2005**, *408*, 131−314.

(7) Hill, M. T.; Gather, M. C. Advances in small lasers. *Nat. Photonics* **2014**, *8*, 908−918.

(8) Knight, M. W.; Sobhani, H.; Nordlander, P.; Halas, N. J. Photodetection with active optical antennas. *Science* **2011**, *332*, 702−704.

(9) Salamin, Y.; Ma, P.; Baeuerle, B.; Emboras, A.; Fedoryshyn, Y.; Heni, W.; Cheng, B.; Josten, A.; Leuthold, J. 100 GHz Plasmonic Photodetector. *ACS Photonics* **2018**, *5*, 3291−3297.

(10) Matsui, J.; Akamatsu, K.; Hara, N.; Miyoshi, D.; Nawafune, H.; Tamaki, K.; Sugimoto, N. SPR sensor chip for detection of small molecules using molecularly imprinted polymer with embedded gold nanoparticles. *Anal. Chem.* **2005**, *77*, 4282−4285.

(11) Taylor, A. D.; Ladd, J.; Yu, Q.; Chen, S.; Homola, J.; Jiang, S. Quantitative and simultaneous detection of four foodborne bacterial pathogens with a multi-channel SPR sensor. *Biosens. Bioelectron.* **2006**, *22*, 752−758.

(12) Min, C.; Shen, Z.; Shen, J.; Zhang, Y.; Fang, H.; Yuan, G.; Du, L.; Zhu, S.; Lei, T.; Yuan, X. Focused plasmonic trapping of metallic particles. *Nat. Commun.* **2013**, *4*, 2891.

(13) Zhang, Y.; Min, C.; Dou, X.; Wang, X.; Urbach, H. P.; Somekh, M. G.; Yuan, X. Plasmonic tweezers: for nanoscale optical trapping and beyond. *Light Sci. Appl.* **2021**, *10*, 59.

(14) Oulton, R. F.; Sorger, V. J.; Zentgraf, T.; Ma, R.-M.; Gladden, C.; Dai, L.; Bartal, G.; Zhang, X. Plasmon lasers at deep subwavelength scale. *Nature* **2009**, *461*, 629−632.

(15) Lu, Y. J.; Wang, C.-Y.; Kim, J.; Chen, H.-Y.; Lu, M.-Y.; Chen, Y.-C.; Chang, W.-H.; Chen, L.-J.; Stockman, M. I.; Shih, C.-K.; Gwo, S. All-color plasmonic nanolasers with ultralow thresholds: autotuning mechanism for single-mode lasing. *Nano Lett.* **2014**, *14*, 4381−4388.

(16) Chou, Y. H.; Chou, B.-T.; Chiang, C.-K.; Lai, Y.-Y.; Yang, C.-T.; Li, H.; Lin, T.-R.; Lin, C.-C.; Kuo, H.-C.; Wang, S.-C.; Lu, T.-C. Ultrastrong Mode Confinement in ZnO Surface Plasmon Nanolasers. *ACS Nano* **2015**, *9*, 3978−3983.

(17) Sidiropoulos, T. P. H.; Röder, R.; Geburt, S.; Hess, O.; Maier, S. A.; Ronning, C.; Oulton, R. F. Ultrafast plasmonic nanowire lasers near the surface plasmon frequency. *Nat. Phys.* **2014**, *10*, 870−876.

(18) Chou, Y. H.; Hong, K.-B.; Chang, C.-T.; Chang, T.-C.; Huang, Z.-T.; Cheng, P.-J.; Yang, J.-H.; Lin, M.-H.; Lin, T.-R.; Chen, K.-P.; Gwo, S.; Lu, T.-C. Ultracompact Pseudowedge Plasmonic Lasers and Laser Arrays. *Nano Lett.* **2018**, *18*, 747−753.

(19) Ma, R. M.; Oulton, R. F. Applications of nanolasers. *Nat. Nanotechnol.* **2019**, *14*, 12−22.

(20) Yang, X.; Ni, P. N.; Jing, P. T.; Zhang, L. G.; Ma, R. M.; Shan, C. X.; Shen, D. Z.; Genevet, P. Room Temperature Electrically Driven Ultraviolet Plasmonic Lasers. *Adv. Opt. Mater.* **2019**, *7*, 1801681.

(21) Pan, Y.; Wang, L.; Su, X.; Gao, D.; Chen, R.; Zhang, Y.; Zhao, Y.; Li, L.; Gao, D. The effectively optical emission modulation in perovskite $MAPbBr_3$ crystal by hot-electron transfer from metals. *J. Phys. D* **2022**, *55*, 375104.

(22) Yang, X.; Shan, Z.; Luo, Z.; Hu, X.; Liu, H.; Liu, Q.; Zhang, Y.; Zhang, X.; Shoaib, M.; Qu, J.; Yi, X.; Wang, X.; Zhu, X.; Liu, Y.; Liao, L.; Wang, X.; Chen, S.; Pan, A. An Electrically Controlled Wavelength-Tunable Nanoribbon Laser. *ACS Nano* **2020**, *14*, 3397−3404.

(23) Li, H.; Huang, Z.-T.; Hong, K.-B.; Hsu, C.-Y.; Chen, J.-W.; Cheng, C.-W.; Chen, K.-P.; Lin, T.-R.; Gwo, S.-J.; Lu, T.-C. Current Modulation of Plasmonic Nanolasers by Breaking Reciprocity on Hybrid Graphene-Insulator-Metal Platforms. *Adv. Sci.* **2020**, *7*, 2001823.

(24) Novoselov, K. S.; Geim, A. K.; Morozov, S. V.; Jiang, D.; Katsnelson, M. I.; Grigorieva, I. V.; Dubonos, S. V.; Firsov, A. A. Two-dimensional gas of massless Dirac fermions in graphene. *Nature* **2005**, *438*, 197−200.

(25) Zhang, Y.; Tan, Y. W.; Stormer, H. L.; Kim, P. Experimental observation of the quantum Hall effect and Berry's phase in graphene. *Nature* **2005**, *438*, 201−204.

(26) Kim, K. S.; Zhao, Y.; Jang, H.; Lee, S. Y.; Kim, J. M.; Kim, K. S.; Ahn, J.-H.; Kim, P.; Choi, J.-Y.; Hong, B. H. Large-scale pattern growth of graphene films for stretchable transparent electrodes. *Nature* **2009**, *457*, 706−710.

(27) Lee, C.; Wei, X.; Kysar, J. W.; Hone, J. Measurement of the elastic properties and intrinsic strength of monolayer graphene. *Science* **2008**, *321*, 385−388.

(28) Balandin, A. A.; Ghosh, S.; Bao, W.; Calizo, I.; Teweldebrhan, D.; Miao, F.; Lau, C. N. Superior thermal conductivity of single-layer graphene. *Nano Lett.* **2008**, *8*, 902−907.

(29) Ghosh, S.; Calizo, I.; Teweldebrhan, D.; Pokatilov, E. P.; Nika, D. L.; Balandin, A. A.; Bao, W.; Miao, F.; Lau, C. N. Extremely high thermal conductivity of graphene: Prospects for thermal management applications in nanoelectronic circuits. *Appl. Phys. Lett.* **2008**, *92*, 151911.

(30) Kim, J.; Son, H.; Cho, D. J.; Geng, B.; Regan, W.; Shi, S.; Kim, K.; Zettl, A.; Shen, Y.-R.; Wang, F. Electrical control of optical plasmon resonance with graphene. *Nano Lett.* **2012**, *12*, 5598−5602.

(31) Hwang, M. S.; Kim, H.-R.; Kim, K.-H.; Jeong, K.-Y.; Park, J.-S.; Choi, J.-H.; Kang, J.-H.; Lee, J. M.; Park, W. I.; Song, J.-H.; Seo, M.-K.; Park, H.-G. Switching of Photonic Crystal Lasers by Graphene. *Nano Lett.* **2017**, *17*, 1892−1898.

(32) Kim, H.; Lee, M.; Jeong, H.; Hwang, M.-S.; Kim, H.-R.; Park, S.; Park, Y. D.; Lee, T.; Park, H.-G.; Jeon, H. Electrical modulation of a photonic crystal band-edge laser with a graphene monolayer. *Nanoscale* **2018**, *10*, 8496−8502.

(33) Li, H.; Li, J.-H.; Hong, K.-B.; Yu, M.-W.; Chung, Y.-C.; Hsu, C.-Y.; Yang, J.-H.; Cheng, C.-W.; Huang, Z.-T.; Chen, K.-P.; Lin, T.-R.; Gwo, S.; Lu, T.-C. Plasmonic Nanolasers Enhanced by Hybrid Graphene-Insulator-Metal Structures. *Nano Lett.* **2019**, *19*, 5017−5024.

(34) Li, H.; Huang, Z.-T.; Hong, K.-B.; Chen, J.-W.; Cheng, C.-W.; Chen, K.-P.; Lin, T.-R.; Gwo, S.-j.; Lu, T.-C. Room-temperature active modulation of plasmonic nanolasers by current injection on hybrid graphene−insulator−metal platforms. *J. Appl. Phys.* **2021**, *129*, 053307.

(35) Fates, R.; Bouridah, H.; Raskin, J.-P. Probing carrier concentration in gated single, bi- and tri-layer CVD graphene using Raman spectroscopy. *Carbon* **2019**, *149*, 390−399.

(36) Chung, Y. C.; Cheng, P.-J.; Chou, Y.-H.; Chou, B.-T.; Hong, K.-B.; Shih, J.-H.; Lin, S.-D.; Lu, T.-C.; Lin, T.-R. Surface roughness effects on aluminium-based ultraviolet plasmonic nanolasers. *Sci. Rep.* **2017**, *7*, 39813.

(37) Cancado, L. G.; Jorio, A.; Martins Ferreira, E. H.; Stavale, F.; Achete, C. A.; Capaz, R. B.; Moutinho, M. V. O.; Lombardo, A.; Kulmala, T. S.; Ferrari, A. C. Quantifying defects in graphene via Raman spectroscopy at different excitation energies. *Nano Lett.* **2011**, *11*, 3190−3196.

(38) Bruna, M.; Ott, A. K.; Ijäs, M.; Yoon, D.; Sassi, U.; Ferrari, A. C. Doping dependence of the Raman spectrum of defected graphene. *ACS Nano* **2014**, *8*, 7432−7441.

(39) Zhu, W.; Perebeinos, V.; Freitag, M.; Avouris, P. Carrier scattering, mobilities, and electrostatic potential in monolayer, bilayer, and trilayer graphene. *Phys. Rev. B* **2009**, *80*, 235402.

(40) Chou, Y.-H.; Chang, C.-J.; Lin, T.-R.; Lu, T.-C. Surface plasmon polariton nanolasers: Coherent light sources for new applications. *Chin. Phys. B* **2018**, *27*, 114208.

https://doi.org/10.1021/acsnano.2c11716
ACS Nano 2023, 17, 6488−6496